



Quantitative region-of-interest tomography using variable field of view

J. C. DA SILVA,^{1,2,*} M. GUIZAR-SICAIROS,¹ M. HOLLER,¹ A. DIAZ,¹ J. A. VAN BOKHOVEN,^{1,3} O. BUNK,¹ AND A. MENZEL¹

¹Paul Scherrer Institut, Villigen PSI, 5232, Switzerland

²Currently with the European Synchrotron Radiation Facility, Grenoble 38000, France

³Institute for Chemical and Bioengineering, ETH Zurich, Zurich, 8093, Switzerland

*jdasilva@esrf.fr

Abstract: In X-ray computed tomography, the task of imaging only a local region of interest (ROI) inside a larger sample is very important. However, without *a priori* information, this ROI cannot be exactly reconstructed using only the image data limited to the ROI. We propose here an approach of region-of-interest tomography, which reconstructs a ROI within an object from projections of different fields of view acquired on a specific angular sampling scheme in the same tomographic experiment. We present a stable procedure that not only yields high-quality images of the ROI but keeps as well the quantitative contrast on the reconstructed images. In addition, we analyze the minimum number of projections required for ROI tomography from the point of view of the band region of the Radon transform, which confirms this number must be estimated based on the size of the entire object and not only on the size of the ROI.

© 2018 Optical Society of America under the terms of the [OSA Open Access Publishing Agreement](#)

OCIS codes: (110.3010) Image reconstruction techniques; (110.6955) Tomographic imaging; (110.6960) Tomography; (110.7440) X-ray imaging.

References and links

1. F. Natterer, *The Mathematics of Computerized Tomography* (SIAM, 2001).
2. R. N. Bracewell and A. C. Riddle, "Inversion of fan-beam scans in radio astronomy," *Astrophys. J.* **150**, 427–434 (1967).
3. A. G. Ramm and A. Katsevich, *The Radon Transform and Local Tomography* (CRC, 1996).
4. M. Müller and G. R. Arce, "Truncation artifacts in tomographic reconstructions from projections," *Appl. Opt.* **35**(20), 3902–3914 (1996).
5. J. C. Gore and S. Leeman, "The reconstruction of objects from incomplete projections," *Phys. Med. Biol.* **25**(1), 129–136 (1980).
6. A. Faridani, E. L. Ritman, and K. T. Smith, "Local Tomography," *SIAM J. Appl. Math.* **52**, 459–484 (1992).
7. A. Faridani, E. L. Ritman, and K. T. Smith, "Local Tomography II," *SIAM J. Appl. Math.* **57**, 1095–1127 (1997).
8. W. J. T. Spyra, A. Faridani, K. T. Smith, and E. L. Ritman, "Computed tomographic imaging of the coronary arterial tree - use of local tomography," *IEEE Trans. Med. Imag.* **9**(1), 1–4 (1990).
9. G. Wang and H. Yu, "Can interior tomography outperform lambda tomography?" *Proc. Natl. Acad. Sci. USA* **107**(22), E92–E93 (2010).
10. R. Bates and R. Lewitt, "Image reconstruction from projections: I: General theoretical considerations, III: Projection completion methods (theory), IV: Projection completion methods (computational examples)," *Optik* **50**, 19–278 (1978).
11. M. Guizar-Sicairos, J. J. Boon, K. Mader, A. Diaz, A. Menzel, and O. Bunk, "Quantitative interior x-ray nanotomography by a hybrid imaging technique," *Optica* **2**(3), 259–266 (2015).
12. F. Pfeiffer, C. David, O. Bunk, T. Donath, M. Bech, G. Le Duc, A. Bravin, and P. Cloetens, "Region-of-Interest Tomography for Grating-Based X-Ray Differential Phase-Contrast Imaging," *Phys. Rev. Lett.* **101**, 168101 (2008).
13. T. Köhler and F. Noo, "Comment on "Region-of-Interest Tomography for Grating-Based X-Ray Differential Phase-Contrast Imaging,"" *Phys. Rev. Lett.* **101**, 039801 (2009).
14. Y. Ye, H. Yu, Y. Wei, and G. Wang, "A general local reconstruction approach based on a truncated Hilbert transform," *Int. J. Biomed. Imaging* **2007**, 63634 (2007).
15. H. Kudo, M. Courdurier, F. Noo, and M. Defrise, "Tiny a priori knowledge solves the interior problem in computed tomography," *Phys. Med. Biol.* **53**, 2207–2231 (2008).
16. K. S. Sharma, C. Holzner, D. M. Vasilescu, X. Jin, S. Narayanan, M. Agah, E. A. Hoffman, H. Yu, and G. Wang, "Scout-view Assisted Interior Micro-CT," *Phys Med Biol.* **58**(12), 4297–4314 (2013).

17. N. Ohyama, A. Shiraishi, T. Honda, and J. Tsujiuchi, "Analysis and improvement in region-of-interest tomography," *Appl. Opt.* **23**(22), 4105–4110 (1984).
18. O. Nalcioglu, Z.H. Cho, and R. Y. Lou, "Limited field of view reconstruction in computerized tomography," *IEEE Trans. Nucl. Sci.* **26**(1), 546–551 (1979).
19. O. Nalcioglu, P. V. Sankar, and J. Sklansky, "Region-of-interest X-ray tomography (ROIT)," *Proc. SPIE* **206**, 98–102 (1979).
20. W. Wagner, "Reconstructions from restricted region scan data - new means to reduce the patient dose," *IEEE Trans. Nucl. Sci.* **26**(2), 2866–2869 (1979).
21. J. C. da Silva and A. Menzel, "Elementary signals in ptychography," *Opt. Express* **23**, 33812–33821 (2015).
22. M. Dierolf, A. Menzel, P. Thibault, P. Schneider, C. M. Kewish, R. Wepf, O. Bunk, and F. Pfeiffer, "Ptychographic X-ray computed tomography at the nanoscale," *Nature* **467**, 436–439 (2010).
23. M. Guizar-Sicairos, A. Diaz, M. Holler, M. S. Lucas, A. Menzel, R. A. Wepf, and O. Bunk, "Phase tomography from X-ray coherent diffractive imaging projections," *Opt. Express* **19**(22), 21345–21357 (2011).
24. T. Olson and J. DeStefano, "Wavelet localization of the Radon transform," *IEEE Trans. Signal Process.* **42**(8), 2055–2067 (1994).
25. T.-C. Hsung and D. P. K. Lun, "New sampling scheme for region-of-interest tomography," *IEEE Trans. Signal Process.* **48**(4), 1154–1163 (2000).
26. M. Guizar-Sicairos, S. T. Thurman, and J. Fienup, "Efficient subpixel image registration algorithms," *Opt. Lett.* **33**, 156–158 (2008).
27. P. A. Rattey and A. G. Lindgren, "Sampling the 2-D Radon transform," *IEEE Trans. Acoust. Speech Signal Process.* **29**(5), 994–1002 (1981).
28. R. A. Crowther, D. J. DeRosier, and A. Klug, "The reconstruction of a three-dimensional structure from projections and its application to electron microscopy," *Proc. Roy. Soc. Lond. A* **317**, 319–340 (1970).
29. A. C. Kak and M. Slaney, *Principles of Computerized Tomographic Imaging* (SIAM, 2001).
30. A. Kyrieleis, V. Titarenko, M. Ibison, T. Connolly, and P. J. Withers, "Region-of-interest tomography using filtered backprojection: assessing the practical limits," *J. Microsc.* **241**(1), 69–82 (2010).
31. J. C. da Silva, K. Mader, M. Holler, D. Haberthür, A. Diaz, M. Guizar-Sicairos, W.-C. Cheng, Y. Shu, J. Raabe, A. Menzel, and J. A. van Bokhoven, "Assessment of the 3D Pore Structure and Individual Components of Preshaped Catalyst Bodies by X-Ray Imaging," *ChemCatChem* **7**(3), 413–416 (2015).
32. X. Xiao, F. de Carlo, and S. R. Stock, "Practical error estimation in zoom-in and truncated tomography reconstructions," *Rev. Sci. Instrum.* **78**(6), 063705 (2007).
33. S. Gorelick, J. Vila-Comamala, V. A. Guzenko, R. Barrett, M. Salome, and C. David, "High-efficiency Fresnel zone plates for hard X-rays by 100 keV e-beam lithography and electroplating," *J. Synchrotron Rad.* **18**, 442–446 (2011).
34. R. Dinapoli, A. Bergamaschi, B. Henrich, R. Horisberger, I. Johnson, A. Mozzanica, E. Schmid, B. Schmitt, A. Schreiber, X. Shi, and G. Theidel, "EIGER: next generation single photon counting detector for X-ray applications," *Nucl. Instrum. Methods Phys. Res. A* **650**, 79–83 (2011).
35. M. Guizar-Sicairos, I. Johnson, A. Diaz, M. Holler, P. Karvinen, H.-C. Stadler, R. Dinapoli, O. Bunk, and A. Menzel, "High-throughput ptychography using Eiger: scanning X-ray nano-imaging of extended regions," *Opt. Express* **22**(12), 14859–14870 (2014).
36. M. Holler, A. Diaz, M. Guizar-Sicairos, P. Karvinen, E. Färm, E. Härkönen, M. Ritala, A. Menzel, J. Raabe, and O. Bunk, "X-ray ptychographic computed tomography at 16 nm isotropic 3D resolution," *Sci. Rep.* **4**, 3857 (2014).
37. M. Holler, J. Raabe, A. Diaz, M. Guizar-Sicairos, C. Quitmann, A. Menzel, and O. Bunk, "An instrument for 3D x-ray nano-imaging," *Rev. Sci. Instrum.* **83**, 073703 (2012).
38. A. P. Kaestner, B. Munch, and P. Trtik, "Spatiotemporal computed tomography of dynamic processes," *Opt. Eng.* **50**(12), 123201 (2011).
39. P. Thibault, M. Dierolf, O. Bunk, A. Menzel, and F. Pfeiffer, "Probe retrieval in ptychographic coherent diffractive imaging," *Ultramicroscopy* **109**, 338–343 (2009).
40. P. Thibault and M. Guizar-Sicairos, "Maximum-likelihood refinement for coherent diffractive imaging," *New J. Phys.* **14**, 063004 (2012).
41. A. Diaz, P. Trtik, M. Guizar-Sicairos, A. Menzel, P. Thibault, and O. Bunk, "Quantitative X-ray phase nanotomography," *Phys. Rev. B* **85**, 020104(R) (2012).
42. A. Guinier, *X-ray diffraction in crystals, imperfect crystals and amorphous bodies* (Dover, 1994).
43. ChemSpider database, "Melanin," (ID 4884931). <http://www.chemspider.com/Chemical-Structure.4884931.html> (data of access February 01, 2018)
44. M. L. Huggins, "The structure of alpha keratin," *Proc. Natl. Acad. Sci. U.S.A.* **43**(2), 204–209 (1957).
45. M. van Heel and M. Schatz, "Fourier shell correlation threshold criteria," *J. Struct. Biol.* **151**(3), 250–262 (2005).

1. Introduction

In X-ray computed tomography, a 3D image of an object is reconstructed from 2D projections taken at multiple angular directions in a range covering 180° in general. The desired 3D image can be reconstructed by applying the inverse Radon transform to the projection dataset [1, 2].

However, the inverse Radon transform in two dimensions leads to artifacts on the reconstructed images from truncated projections limited to the region of interest (ROI) of a larger sample, which in turn hampers the extraction of quantitative information from the reconstructed image gray level [1, 3–5]. This implies that the entire object has to be imaged to allow the exact recovery of the ROI, thus increasing the duration of the experiments and hampering the capability to zoom into a ROI with higher resolution.

Several approaches have been proposed to deal with this issue in ROI tomography reconstructions. Lambda-tomography [6–8] can recover gradient-like features within a ROI from truncated projections, but the reconstructed images are non-quantitative [9]. Sinogram truncation artifacts can be significantly reduced by padding the sinograms with the edge value [10], an approach called sinogram extension, which is mathematically equivalent to a computation from truncated differential data [11, 12]. However, while this approach reduces the artifacts, the reconstruction remains non-quantitative [13]. An exact reconstruction is only possible if some prior information about the ROI is available [14, 15].

Instead of dealing with only truncated data, some approaches which have been proposed are based on dual sampling and dual reconstruction followed by data completion [16–20]. The idea behind these methods is measuring conventional projections covering the entire object with reduced resolution and moderately higher-resolution interior projections limited to the ROI. The latter results in truncated sinograms that are completed with the lower-resolution sinograms and fed to a conventional tomographic reconstruction routine. In this manner, the interior region can be reconstructed with significantly reduced truncation artifacts and with quantitative contrast.

These techniques are mainly motivated by limitations of conventional imaging systems, such as a finite number of pixels in the detectors. For scanning microscopy techniques, the field of view is not limited by the detector size, but by the scanning range. Ptychography is a coherent imaging technique working in scanning microscopy mode which is capable of providing highly detailed and quantitative images of a sample's complex-valued transmittance [21]. Ptychographic X-ray computed tomography (PXCT) [22, 23] is the combination of ptychography and tomography which yields quantitative 3D maps of the complex-value refractive index of the sample [22]. For X-rays, the refractive index is given by $n = 1 - \delta + i\beta$, where δ is the refractive index decrement and β is the absorption index. However, this quantitative capability of PXCT is lost in case of ROI tomography.

There is a recent approach in which ptychographic interior nanotomography with quantitative contrast is achieved by numerical combination of high-resolution interior projections with a coarse overview tomogram, both acquired separately [11]. Rather than patching truncated sinograms, an optimization algorithm was previously developed to combine the two measurements in 3D [11]. An upsampled version of the overview tomogram is fed to this optimization algorithm, and the volume is refined to match the high-resolution ptychographic projections. The technique was demonstrated to an interior reconstruction of 130 nm resolution obtained with ptychographic projections and an overview tomogram at 1 μm resolution, and it was used to characterize the 3D arrangement of nanometer-scale vesicles in avian eggshell and to recover quantitatively the expected density of bio-calcite to within 3 % of its tabulated value [11]. The method relies on iterative reconstruction and it was shown to be robust and accurate, however the upsampling of the overview tomogram can introduce errors as a function of the chosen interpolation method.

In the present work, we introduce an approach of Pseudo Region-of-Interest Tomography capable of overcoming these problems, which we will abbreviate P_{Ro}IT for the remainder of this text. We used the word “pseudo” because projections covering the entire object are also acquired in a sparse angular sampling along with localized projections of the region-of-interest. The approach is inspired by the multiresolution method proposed by Olson and DeStefano [24]. In this approach projections covering different fields of view are measured in the same experiment as schematically shown in Fig. 1, such that non-truncated projections are only acquired in a sparse

angular sampling grid whereas the ROI is measured with fine angular sampling. This method allows for measurements of a ROI with arbitrary diameter within the object while preserving quantitative contrast. It can exploit, for example, the scanning modality of microscopy techniques such as ptychography, scanning transmission X-ray microscopy (STXM) and X-ray fluorescence tomography to alternate the sizes of the fields of view at each angle.

The remainder of this paper is structured as follows. Section 2 describes the P_{ROI}IT method, including radial and angular samplings, alignment and interpolation of the projections of different levels. Numerical simulations with the Shepp-Logan head phantom are considered in Section 3 to evaluate the role of the level decomposition, to compare to P_{ROI}IT to the classical ROI tomographic reconstruction method of sinogram extension, and to estimate the minimum number of projections required from the point-of-view of the bowtie-like band region of the Radon transform. The performance of P_{ROI}IT is tested against experimental data in two ways: (i) using digitally truncated experimental projections of a catalyst particle in Section 4; and (ii) carrying out a P_{ROI}IT experiment to reconstruct a ROI within a hair shaft using X-ray ptychography to acquire the projections in Section 5. We conclude with Section 6.

2. Pseudo region-of-interest tomography (P_{ROI}IT)

2.1. Projection acquisition scheme

In the P_{ROI}IT approach, the object is scanned with projections of variable sizes in a specific angular sampling scheme. Figure 1 illustrates the scheme of projection acquisition in which full size projections are acquired in a coarsely sampled angular range and smaller projections are taken for the intermediate angles. In this example, the ROI is located in the center for simplicity, but it can also be off-centered. The projections of different sizes are obtained in subsets of stacks called levels as illustrated in Fig. 1(a), and a schematic representation over the corresponding sinogram is displayed in Fig. 1(b).

Four levels are showed here for clarity, but this number can be adjusted to a different number of levels if needed. The minimum number of levels is two, but more levels will help the transition from the ROI imaging to the exterior region. The level L₃ consists of full projections sized $2 \times \ell_3$ covering the entire object, which is necessary to obtain quantitative information of the object. The level L₀ comprises the truncated projections sized $2 \times \ell_0$, which corresponds to the ROI size. The intermediate levels, L₁ and L₂, sized $2 \times \ell_1$ and $2 \times \ell_2$ respectively, are used for a better reconstruction of the ROI. The projections are distributed over the levels in the following way: 1/8 of the projections are L₃, 1/8 are L₂, 1/4 are L₁, and 1/2 are L₀. This structure of levels is inspired by the multiresolution analysis using wavelets in tomography previously proposed [24], but with relaxed sampling condition for the size of each level. Later on, it was showed that a linear interpolation of the projections could yield results at least as good as those achieved by using the wavelets approach and that the reconstruction quality is largely determined by the use of an appropriate angular sampling pattern [25].

Compared to previous works on dual sampling and dual reconstruction, P_{ROI}IT offers the advantage of acquiring the projections of variable fields of view in the same experiments in a specific angular sampling strategy. All projections have the same rotation axis, spatial resolution and pixel size, which facilitate the alignment of the projections and interpolation of the missing information. Due to the coarse angular sampling, the overview tomogram using only the L₃ projections is of low resolution, but it is quantitative. When combining such a low-resolution overview with the other levels, the angular distribution of projections is not undersampled anymore. Consequently, we can reconstruct a high resolution image of the ROI which allows us to accurately quantify the electron density of the sample within the ROI. In addition, we can fully customize the field of view of the different levels as needed using scanning microscopy techniques such as X-ray ptychography [21–23], which is relatively slow due to its scanning nature. Therefore, P_{ROI}IT offers the option of acquiring less data via reduction of the field of view,

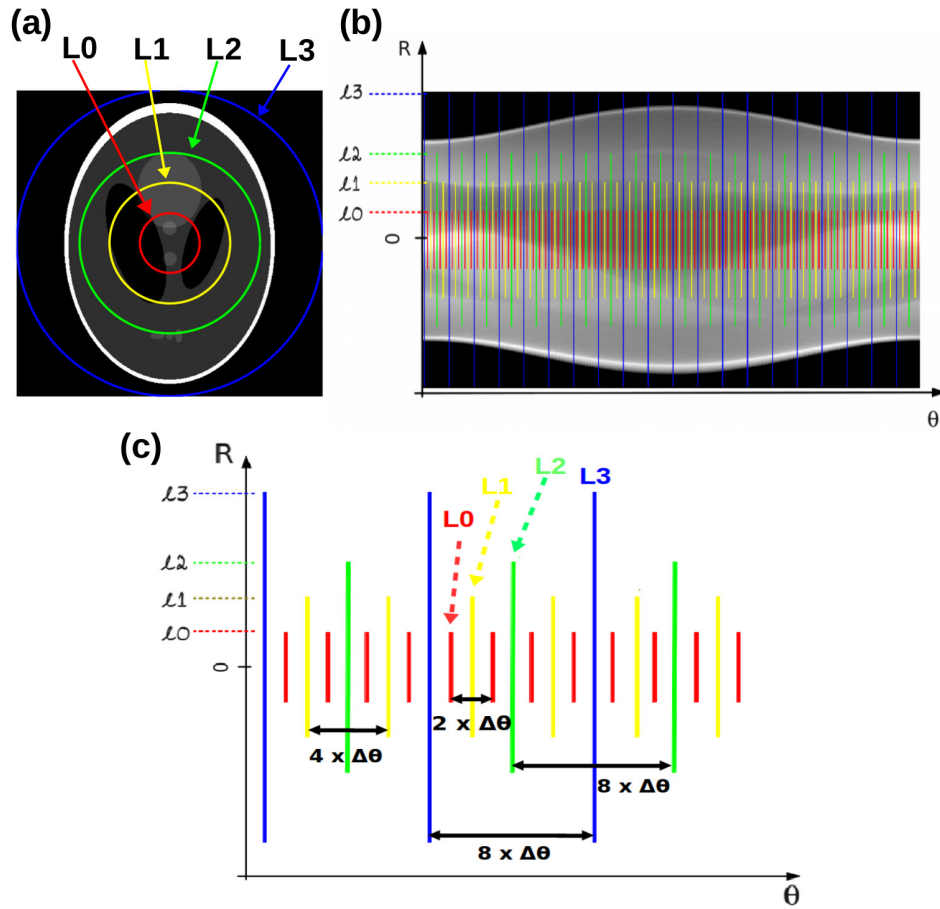


Fig. 1. Schematic representation of the PProFIT approach. (a) Shepp-Logan head phantom where the different sizes of the regions in different levels, named L0 (ROI), L1, L2, and L3. (b) The corresponding sinogram where the different levels are indicated by colors. The size of the projections are $2\ell_0$, $2\ell_1$, $2\ell_2$, and $2\ell_3$ for the levels L0, L1, L2 and L3, respectively, and are related to the colored circles in (a). (c) Angular sampling of the different levels. Each level contains equally spaced projections in the angular range. Their spacings are indicated and $\Delta\theta$ is the angular resolution when combining all the levels.

which can decrease the duration of the experiment relative to the conventional PXCT experiments. Additionally, although the ROI receives the same dose as in conventional tomography, PProFIT reduces the dose outside of the ROI.

2.2. Radial and angular sampling

Figure 1(c) illustrates the angular distribution of the projections for each level. Let $\Delta\theta$ be the angular step and θ_1 be the first angle. Let us also define the tomographic angles for the levels as θ_{L0} , θ_{L1} , θ_{L2} , and θ_{L3} . Thus, the angular sampling for each level can be generalized as:

$$\begin{aligned}
\theta_{L0}^{(n)} &= \theta_1 + (2n - 1) \Delta\theta, \\
\theta_{L1}^{(n)} &= \theta_1 + (4n - 2) \Delta\theta, \\
\theta_{L2}^{(n)} &= \theta_1 + (8n - 4) \Delta\theta, \\
\theta_{L3}^{(n)} &= \theta_1 + (8n - 8) \Delta\theta,
\end{aligned} \tag{1}$$

where n is a natural number representing the projection number and such that $0 \leq n \leq M$, where M is the total number of projections. This angular distribution provides subsets of projections for each level which are equally spaced in angles if M is a multiple of 8, which could be individually used for tomographic reconstruction if needed. In case of only two levels, the subsets of angles $\theta_{L1}^{(n)}$ and $\theta_{L2}^{(n)}$ are included in the level $L0$.

Concerning the radial sampling, the width of the $L0$ projections is defined by the size of the ROI and the size of the $L3$ projections is given by the total width of the sample plus a small area around. For the decomposition of the dataset in only two levels, the width of the $L1$ and $L2$ projections is the same as the width of the $L0$ projections, i.e., the ROI size. In this way, we only need to define the sizes of the $L1$ and $L2$ projections for the 4-level case, which are given by:

$$\begin{aligned}
\ell_1 &= \ell_0 (1 + k), \\
\ell_2 &= \ell_1 (1 + k),
\end{aligned} \tag{2}$$

where k can take any positive real number whose value depends on many factors, including the the signal-to-noise ratio of the images, the sample contrast, possible angular undersampling and others. This means that its value needs to be chosen according to the experimental conditions for each sample. At the present work, we chose values between 0.25 and 1 for k . Therefore, the search for its optimum value is out of the scope of this work and has to be investigated in a future work.

2.3. Alignment and interpolation of the projections of different levels

The projections obtained in all the levels are high resolution 2D images. However, the $L3$ projections, for example, are sparsely sampled in the angular range. Those projections are aligned and used to calculate a low-resolution tomogram of the sample in a standard reconstruction [1, 22, 23]. Afterwards, we interpolate the coarsely angular sampled stack of level $L3$ projections from the entire object to the fine angular sampling using a linear interpolation. In case of phase contrast imaging techniques such as ptychography, prior to the interpolation, the phase shifts and the linear phase ramp of the ptychographic projections, corresponding to a constant and linear phase term, are corrected as described in [23]. The regions of the interpolated projections at the angles corresponding to the $L0$, $L1$ and $L2$ projections are replaced by the measured ones.

The $L0$, $L1$ and $L2$ projections need to be aligned to the stack of projections interpolated from the $L3$ projections and their phase shifts need to be corrected. This is done iteratively in two steps: (i) the constant and linear phase difference between each truncated projection and the corresponding interpolated one are calculated using the subpixel cross correlation algorithm described in [26]. (ii) the $L0$, $L1$, $L2$ projections are aligned to the corresponding interpolated projections from level $L3$ using a variation of the gradient descent method, i.e., the direction of decrease of the RMS errors within the area of the truncated projections is searched by allowing the projections to move either zero or one pixel each time. If the RMS error is reduced the step is accepted and this is repeated iteratively until no changes in the RMS errors are observed anymore. Afterwards, the combined stack is used to perform the reconstruction using the filtered backprojection (FBP) algorithm [2, 23].

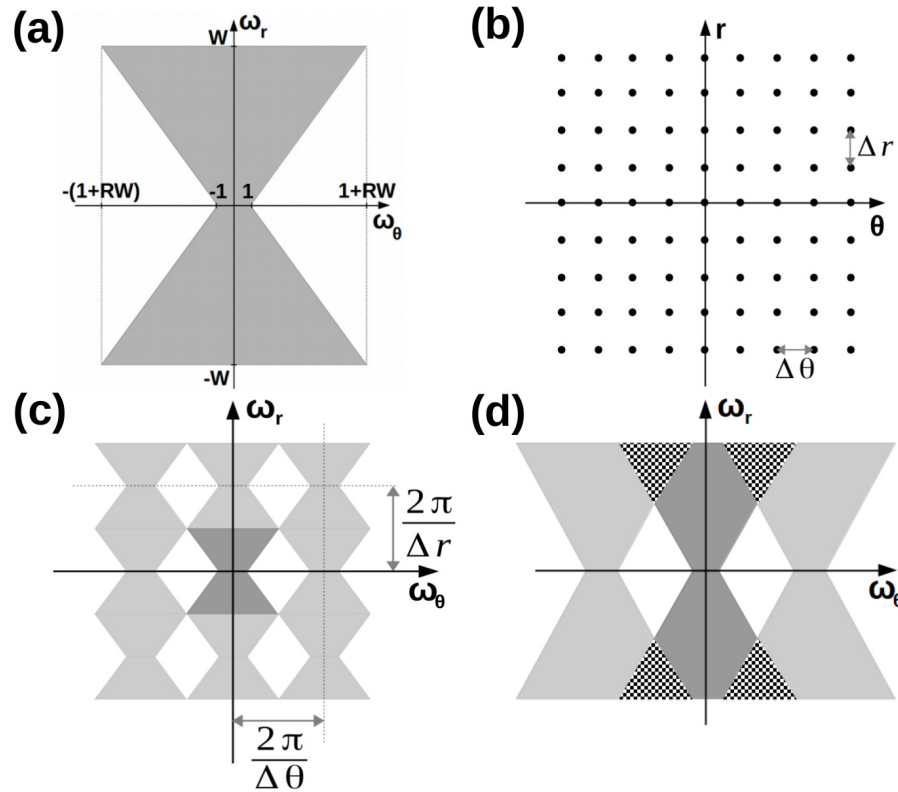


Fig. 2. The bowtie-like band region of the Radon transform. (a) The representation of the band region of the Radon transform of an object of size $2 \times R$ and maximum spatial frequency W . This band region is called RW-bowtie and is obtained by the Fourier transform of the sinogram. The slope of the limits of the bowtie-like band region depends on $1/R$. (b) Sampling of the projections in a rectangular grid with Δr in the radial direction and $\Delta \theta$ in the angular direction. (c) Representation of the discrete Fourier transform of the rectangularly sampled Radon transform of (b) generated from equispaced projections from 0 to π . Periodic replications of the RW-bowtie will appear and proper angular sampling is needed to avoid aliasing errors. (d) Representation of the aliasing errors affecting the bowtie-like band region of the Radon transform in case of angular undersampling. The affected areas are illustrated by checkerboard regions.

3. Numerical simulations with the Shepp-Logan head phantom

3.1. Minimum number of projections for PROFIT

One of the questions concerning the tomographic reconstruction from truncated projections is the minimum number of projections one needs to acquire to avoid aliasing errors, namely the proper angular sampling for the reconstruction. Here, we analyze this problem from the point of view of the band region of the Radon transform, i.e., the 2D Fourier transform support of the sinogram, which has a bowtie-like shape [27]. For a brief recapitulation of the concept, a representation of the band region of the Radon transform of an object supported in a circular region of radius R is displayed in Fig. 2(a). As a consequence of the rectangular sampling of the data in the radial (r) and angular (θ) axes in the sinogram space illustrated in Fig. 2(b), the bowtie-like shape support replicates itself on both the ω_θ and ω_r axes in Fourier domain as shown in Fig. 2(c) [1, 25, 27].

The maximum radial frequency of the object in the Fourier space is $W = \pi/\Delta r$, where Δr is the

real space radial sampling resolution. Accordingly, the angular step for the projection acquisition should be $\Delta\theta < \pi/(RW + 1)$ to avoid aliasing errors, which implies that the number of projections should be $M > \pi/\Delta\theta = \pi \times (R/\Delta r) + 1$ [27]. Thus, for an object of size $D = 2 \times R$, the required minimum number of projections is given by the relation $M > (\pi/2) \times (D/\Delta r) + 1$ or equivalently:

$$M > \frac{\pi}{2} \times N + 1, \quad (3)$$

where N is the number of radial samples (pixels or resolution elements) along the entire object in each projection. Apart from the term $+1$, this relation is similar to the one derived by calculating the minimum number of projections which gives the same radial and angular sampling steps, which is $M > (\pi/2) \times N$ [28, 29]. Since we usually have to deal with a large number of radial samples, $N \gg 1$, these two relations are equivalent. However, in the case Eq. 3 cannot be respected and the angular range is undersampled, aliasing errors will affect the bowtie-like band region of the Radon transform. Figure 2(d) illustrates such a situation where the aliased area are displayed by checkerboard regions. We can immediately see the high spatial frequencies ω_r are the most affected, which implies that the reconstructed tomographic slice will be of lower resolution than the one reconstructed from projections with proper angular sampling.

3.2. Role of the intermediate levels in PProfIT and comparison to reconstruction method of sinogram extension

Simulations of the PProfIT approach were performed using the Shepp-Logan head phantom of 512×512 pixels as shown in Fig. 1. The support size of the head phantom was $N = 470$ pixels and the projections were decomposed in 4 levels: L0, L1, L2 and L3. Since the minimum number of projections required, as described in Section 2, must be larger than $(\pi/2) \times N + 1 \approx 738$, we chose to simulate 744 projections. This number is a multiple of 8, which allows an uniform distribution of the four levels projections over the 180° -range. Following the distribution of projections over the levels as described in Section 2, the simulated dataset (i) was composed of 93 level L3 projections 512 pixels wide, 93 level L2 projections 288 pixels wide, 186 level L1 projections 164 pixels wide, and 372 level L0 projections 94 pixels wide, which corresponds to the diameter of circular ROI as represented by L0 in Fig. 1. The ROI represents about 20 % of the sample support and the sizes of the L1 and L2 projections were given by Eq. (2) with $k=0.75$. The tomographic reconstructions were performed using the filtered back projection algorithm with Hanning filter. In order to assess the gain in using four levels rather than the main two levels (L0 and L3), we have also performed the reconstruction using 2-level decomposition, where the size of the projections from levels L1 and L2 was the same as the ones from level L0.

Figures 3(a) and 3(b) show the reconstructed slices from the projections distributed in four and two levels, respectively. Figure 3(c) shows the reconstructed slice from only truncated projections and using the sinogram extension approach [10]. In addition, we also reconstructed the phantom using non-truncated projections and standard tomographic reconstruction (not shown), which we used as ground-truth for comparison. Figures 3(d), 3(e) and 3(f) display the absolute value of the difference between such a ground-truth image and the PProfIT reconstructions with four and two levels, and the sinogram extension reconstruction, respectively. An offset of 9×10^{-3} was added to the gray level values of the sinogram extension reconstruction due to its intrinsic loss of the quantitative information, which we could retrieve thanks to the reconstructions by conventional tomography and PProfIT. The reconstruction with PProfIT does not suffer from the offset difference because the quantitative information is not lost during the reconstruction.

The RMS errors calculated using only the pixels within the ROI were 1.4×10^{-3} for the reconstruction using PProfIT with four levels, 3.3×10^{-3} for the reconstruction with two levels, and 1.4×10^{-2} for the reconstruction using sinogram extension. This already indicates an improvement in the reconstructed ROI with four levels relative to the one with only the two main levels and a significant improvement of PProfIT reconstruction relative to the sinogram extension

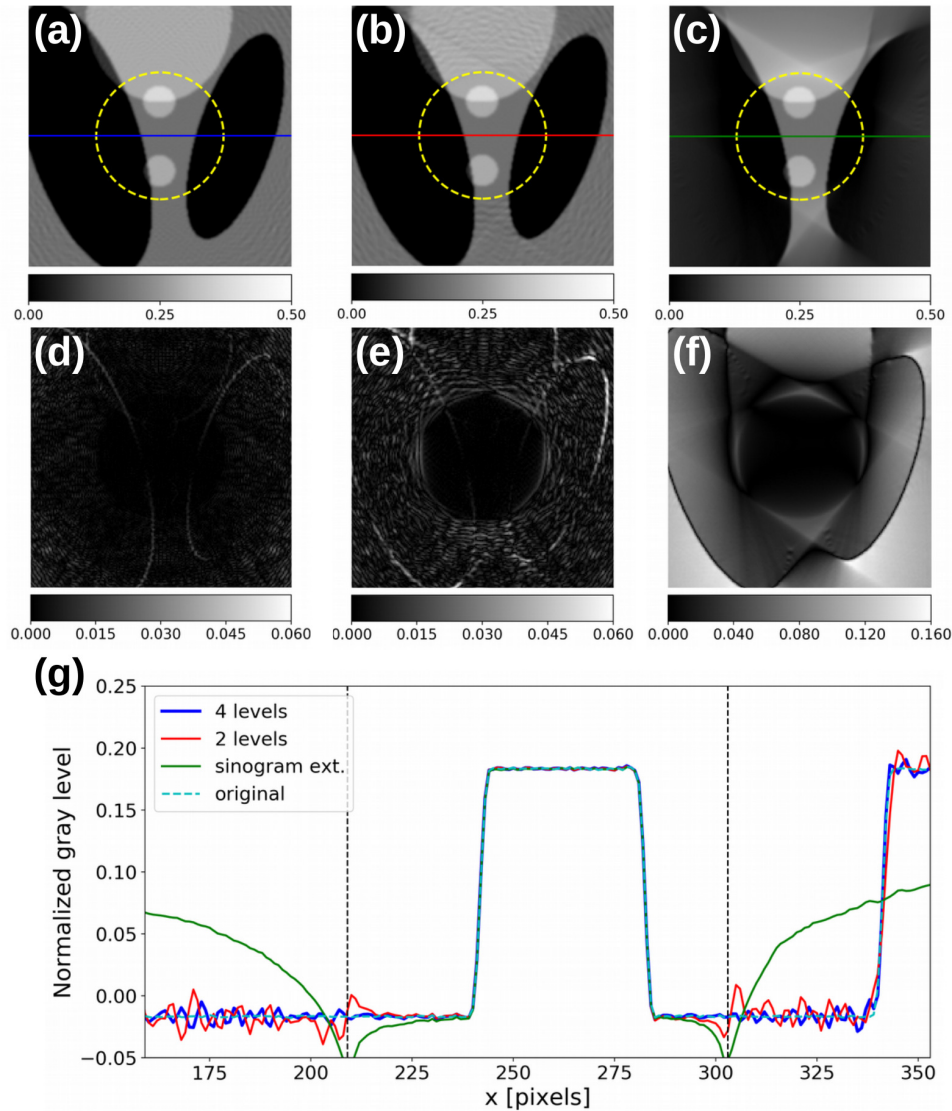


Fig. 3. Results of the simulations with the Shepp-Logan head phantom using PProFIT approach. Tomographic reconstruction using (a) 4-level projections, (b) 2-level projections, and (c) only truncated projections and the sinogram extension approach. An offset of 9×10^{-3} was added to the gray level in (c) to compensate for the loss of quantitative contrast of the approach. The images of the absolute value of the difference between the original tomographic reconstruction from non-truncated projections and the reconstruction in (a), (b), and (c) are shown in (d), (e), and (f), respectively. The images are zoomed-in of the ROI (dashed yellow lines) with a region around the transition from the region away the ROI to the ROI. (g) The gray level profiles across the blue, red, and green lines in (a), (b), and (c), respectively, along with the one from the original reconstruction from non-truncated projections. The dashed black lines limit the region-of-interest.

reconstruction. Figure 3(g) shows the gray level profiles across the blue, red and green lines in Figs. 3(a), 3(b) and 3(c), respectively, and one across the ground-truth image. Except for the additional gray level correction we applied to the reconstructed image using sinogram extension,

its profile agrees relatively well with the other reconstructions within the ROI.

We can also see from Fig. 3(g) that the differences between the P_{RoFIT} reconstructions with four levels and two levels appear mostly at the border of the reconstructed ROI. This happens because the transition for coarsely angular sampled projections from level L3 is too abrupt, specially when using only linear interpolation. Thus, the intermediate levels assist the gradual interpolation from the region away from the ROI to the ROI and allow a reconstruction of better image quality. Undoubtedly, one can still use only two levels when necessary without losing the quantitative capability of the method.

3.3. Bowtie-like band region of the Radon transform

In the first column of Fig. 4, the sinograms of the four subsets of projections are shown. These subsets are all undersampled in the angular range. In the second columns of Fig. 4, the discrete Fourier transform of the corresponding sinograms are presented, where we readily notice the aliasing in the bottom and top parts of the band regions. Before the discrete Fourier transform, the sinograms were multiplied by the Hanning window function in the radial direction to attenuate truncation effects in the radial spatial frequencies ω_r . The angular frequencies ω_θ are not affected because the sinogram truncation is only radial. The band regions of levels L2 in Fig. 4(h) and L3 in Fig. 4(k) are the most affected ones because there are fewer projections in these levels than in the levels L1 in Fig. 4(e) and L0 in Fig. 4(b), which are also affected by aliasing despite the different sizes of the projections. Note that the coordinates of the ω_θ axes change in the figure to adapt to the proper Fourier sampling. In the third columns of Fig. 4, the band regions for the case in which the number of projections is increased to the required number for the entire object support are presented. We notice that the artifacts disappeared albeit there are some missing frequencies due to the truncation of the projections. Figure 4(l) represents the case in which the sampling requirements are respected and the projections cover the entire object. Note the range of the ω_θ axes is now the same for all band regions.

Since the slope of the limits of the bowtie-like band region, given by $W/(1 + RW - 1) = 1/R$, depends on the inverse of the size of the entire object and not on the size of the ROI as previously illustrated in Fig. 2, by reducing the number of projections, the ends of the bowtie regions will give rise to the observed aliasing errors independently of the size of the projections. In addition, given that the maximum frequency W depends on the radial sampling resolution Δr and not on the object size D , the truncation of the projections will not affect the maximum radial frequency of the 2D polar Fourier transform of the Radon transform. Therefore, the total number of projections in the P_{RoFIT}, including all levels, must be equal or higher than the number of projections that would be required for the non-local tomography to avoid aliasing due to the angular sampling. This conclusion is also supported by a previous work on ROI computed tomography [30].

4. P_{RoFIT} using digitally truncated PXCT projections

In order to compare the non-truncated reconstruction and the P_{RoFIT} reconstruction of the same dataset and to exemplify the P_{RoFIT} approach, we digitally truncated the 450 experimental projections from a previous conventional PXCT experiment carried out on a fluid catalytic cracking (FCC) catalyst [31]. The original field of view of the projections was $13 \times 11 \mu\text{m}$ (horizontal \times vertical) and the pixel size was 14.3 nm. We created the four levels of projections by truncating the images as schematically shown in Fig. 5. The regions representing the different projection levels are indicated by colored rectangles.

In order to apply the alignment and interpolation described in Section 2.3, we truncated the original projections before the alignment. For simplicity, the vertical size of the projections here was chosen to be $2.77 \mu\text{m}$. The vertical size of the L3 projections was $3.49 \mu\text{m}$ before the alignment of the projections and were cropped to $2.77 \mu\text{m}$ afterwards. The horizontal sizes were $2.72 \mu\text{m}$ for level L0, $3.44 \mu\text{m}$ for level L1, $4.15 \mu\text{m}$ for level L2, $11.30 \mu\text{m}$ for level L3. We

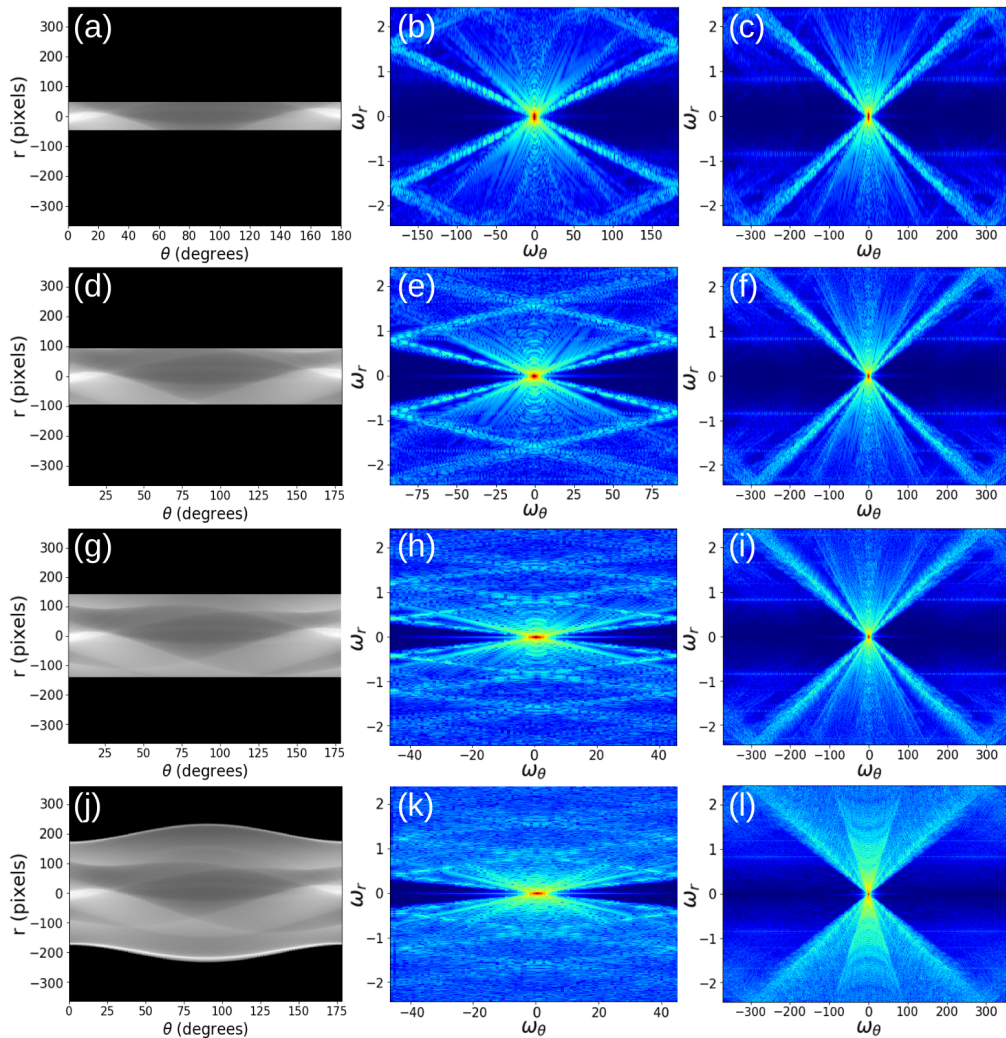


Fig. 4. The RW-bowtie shaped support of the 2D Fourier transform of the Radon transform for the 4-level decomposition of the sinogram. The different sinograms corresponding to the levels L0 (372 projections), L1 (186 projections), L2 (93 projections) and L3 (93 projections) are shown in (a), (d), (g), and (j), respectively. They are undersampled in the angular range. The RW-bowtie support for each of this level of decomposition is shown in (b), (e), (h) and (k) for L0, L1, L2 and L3 projections, respectively. In the third column, the RW-bowtie support for each level is shown again, but this time with a finer angular sampling considering the entire object size according to Eq. (3).

used a value of $k = 0.25$ in Eq. 2. The horizontal size of the ROI represents about 35 % of the sample support and the horizontal sizes of the L1 and L2 projections were about 1.25 \times and 1.5 \times larger than the ROI, respectively. We distribute the 450 projections originally acquired in a standard PXCT experiment in the 4 levels as follows: 225 projections for L0, 112 for L1, 56 for L2, and 57 for L3.

Using the conventional reconstruction with the non-truncated projections, one slice from the 3D images of the FCC catalyst is shown in Fig. 6(a), whereas using the PProfIT approach with four levels we obtain the tomographic slice as shown in Fig. 6(b). For comparison, Fig. 6(c) shows the

reconstructed slice using the sinogram extension approach from only truncated projections with the size of the L0 projections. Then, a modified filtered back projection to work with differential data was used to reconstruct the tomographic slice from the projection derivatives [12, 23]. The ROI is indicated by a yellow dashed circles in Fig. 6(a), 6(b) and 6(c). Figures 6(d), 6(e) and 6(f) display zoomed-in images of the reconstructed slices containing the ROI and also part of the region away from the ROI to better visualization the transition between the two regions and the improved quality of the ROI. We also performed a Fourier Shell Correlation using only the reconstructed ROI as shown in the Appendix A. We found a similar value of 39 nm for the ground truth, PRefIT and sinogram extension reconstruction, which was expected since the three datasets contain the same number of projections. All those reconstruction have the same pixel size of 14.3 nm. This also demonstrates that PRefIT does not degrades the spatial resolution relative to the conventional tomography.

Figure 6(g) shows the gray level profile taken through the blue line in Fig. 6(a), which is plotted along with the one through the red line in Fig. 6(b) and the one through the green line in Fig. 6(c). We immediately notice the similarity between the two profiles in the ROI and even away from the ROI for the conventional reconstruction and PRefIT, despite some blurring of the latter. This indicates that within the ROI the image obtained with PRefIT agrees quite well with the one obtained by non-local tomography. Additionally, the quantitative information encoded in the gray level is preserved. One can also observe the absence of the typical artifacts of local tomography reconstruction, e.g. cupping effect or gray level offset, within the ROI [1, 30, 32]. Figure 6(g) also shows that, despite a gray level offset, the profile obtained from the reconstruction using sinogram extension agrees well with the conventional reconstruction within the ROI, but is very different away the ROI. Such a profile had been corrected by an offset of 0.65×10^{-5} added to the gray level values due to the loss of the quantitative information intrinsic of the sinogram extension reconstruction. This is a good example of the robustness of PRefIT to keep the quantitative contrast in the reconstructed tomogram.

5. Experimental demonstration in a hair shaft

In order to test PRefIT experimentally, we performed an experiment with the tip of a black-hair shaft whose oval cross-section was about $80 \times 60 \mu\text{m}$ in size. We aim at demonstrating that we can image only a ROI within the hair, in our case, we were interested in imaging the outer cuticles together with a part of the cortex in a off-centered region of the hair.

The PRefIT experiment was performed at the coherent X-ray scattering beamline cSAXS at the Swiss Light Source, Paul Scherrer Institut, Switzerland. The photon energy was set to 6.2 keV using a double-crystal Si(111) monochromator. The experiment was carried out with two levels of projections. 600 projections were acquired in total from which 150 projections of $86 \times 15 \mu\text{m}$ ($H \times V$) covered the entire sample width. The remaining 450 projections covered the ROI only, which was of $26 \times 15 \mu\text{m}$ ($H \times V$). The ROI was chosen to be located off-center and enclosed part of the hair cuticles. The aperture of X-ray slits located about 22 m upstream the sample was set to $20 \mu\text{m}$ to increase the horizontal transverse coherence of the X-ray beam. The illumination onto the sample was defined by a gold Fresnel zone plate (FZP), fabricated at the Laboratory for Micro and Nanotechnology (LMN) at PSI, whose diameter was $170 \mu\text{m}$ and outermost zone width was 60 nm [33]. The sample was placed 2.7 mm downstream of the FZP focus resulting in an illumination probe size at the sample of about $9 \mu\text{m}$. The coherent diffraction patterns were acquired using an EIGER detector [34, 35] with pixel size of $75 \mu\text{m}$ placed 7.36 m downstream of the sample. A He-flushed tube was positioned between the sample and the detector to reduce air scattering and absorption. The measurements were carried out using the instrumentation for high-precision nanopositioning of sample described in previous works [36, 37].

The projections were acquired using a binary acquisition strategy [38] with 8 nests of projections, as discussed in section 2.1. Each projection was obtained by a ptychographic scan of

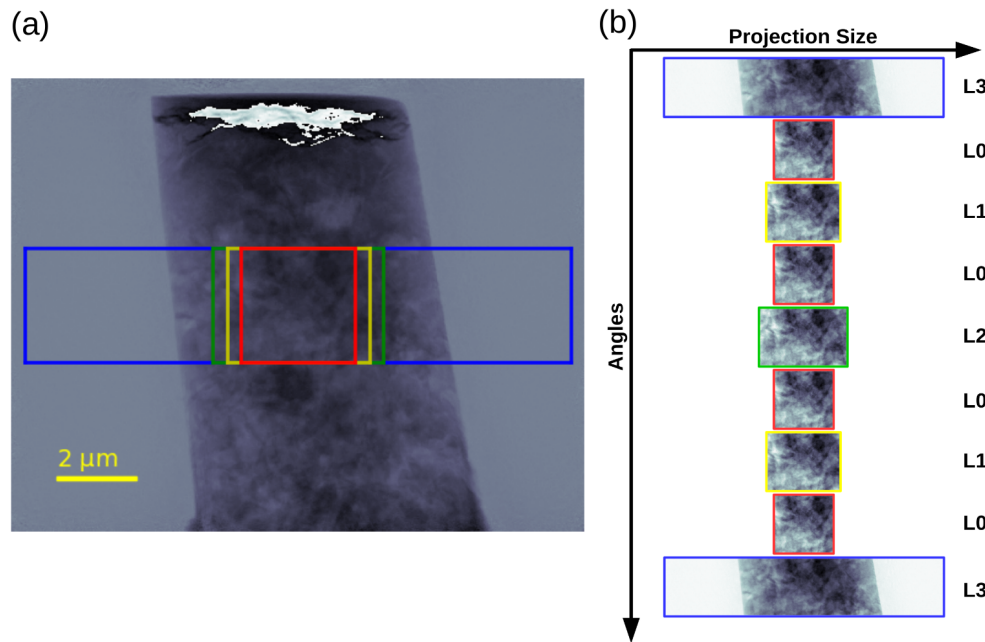


Fig. 5. Representation of the digital truncation of the PXCT projections of a FCC catalyst sample. (a) One phase projection acquired from the pillar porous material where the 4 colored square regions represent a 4-level decomposition for PProFIT. Blue for L3, green for L2, yellow for L1, and red for L0. (b) A representation of the set of truncated projections for the 4 levels. The levels are indicated on the right side of each projection.

129 diffraction patterns with an exposure time of 0.1 seconds each. In order to avoid a pathology which can be caused by a periodic scan grid [39], the sampling positions lay on circular shells with a radial step size of $3\ \mu\text{m}$ and with 5 equally spaced points in the first inner shell. This gives a sampling ratio of $1/\alpha\gamma = 6.54$, where $\alpha = 0.33$ is the ratio step-size/beam-size and $\gamma = 0.46$ is the inverse of the oversampling factor in the reciprocal space, which respects the sampling requirements of ptychography ($1/\alpha\gamma > 1$) [21]. From each diffraction pattern, a region of 400×400 pixels was used in the reconstructions, resulting in a pixel size of $49.3\ \text{nm}$ in the reconstructed projections. Each reconstruction was obtained with 1600 iterations of the difference map algorithm [39] followed by 100 iterations of maximum likelihood refinement [40]. Prior to the tomography reconstructions, the projections were processed according to the procedure described in Section 2. The tomographic reconstruction was performed using a modified filtered backprojection algorithm (FBP) suitable for wrapped phase with a Hanning filter [23].

Figure 7(a) shows the reconstructed image using the PProFIT approach in which the ROI is highlighted by a solid yellow circle. Figure 7(b) displays the ROI, where some parts of the cuticle scales, the cortex, and some grains of melanin are indicated. Figure 7(c) shows the gray level profile across the solid blue line on Fig. 7(a), where we do not observe any of the typical local tomography artifacts. Also, the peak indicated by an arrow shows the gray level value when crossing a grain of melanin. In addition to the high resolution images of the ROI, Fig. 7 shows that PProFIT also provides a reconstruction of the region outside the ROI with lower resolution. Given that the reconstructed image preserves the quantitative information, the electron density can be obtained, from which the mass densities can be estimated [41]. We obtained the following values of mass densities (ρ): $1.3 \pm 0.2\ \text{g/cm}^3$ for the hair cortex and $1.6 \pm 0.2\ \text{g/cm}^3$ for the melanin grains. Since the exact chemical composition of these components are unknown, the values of

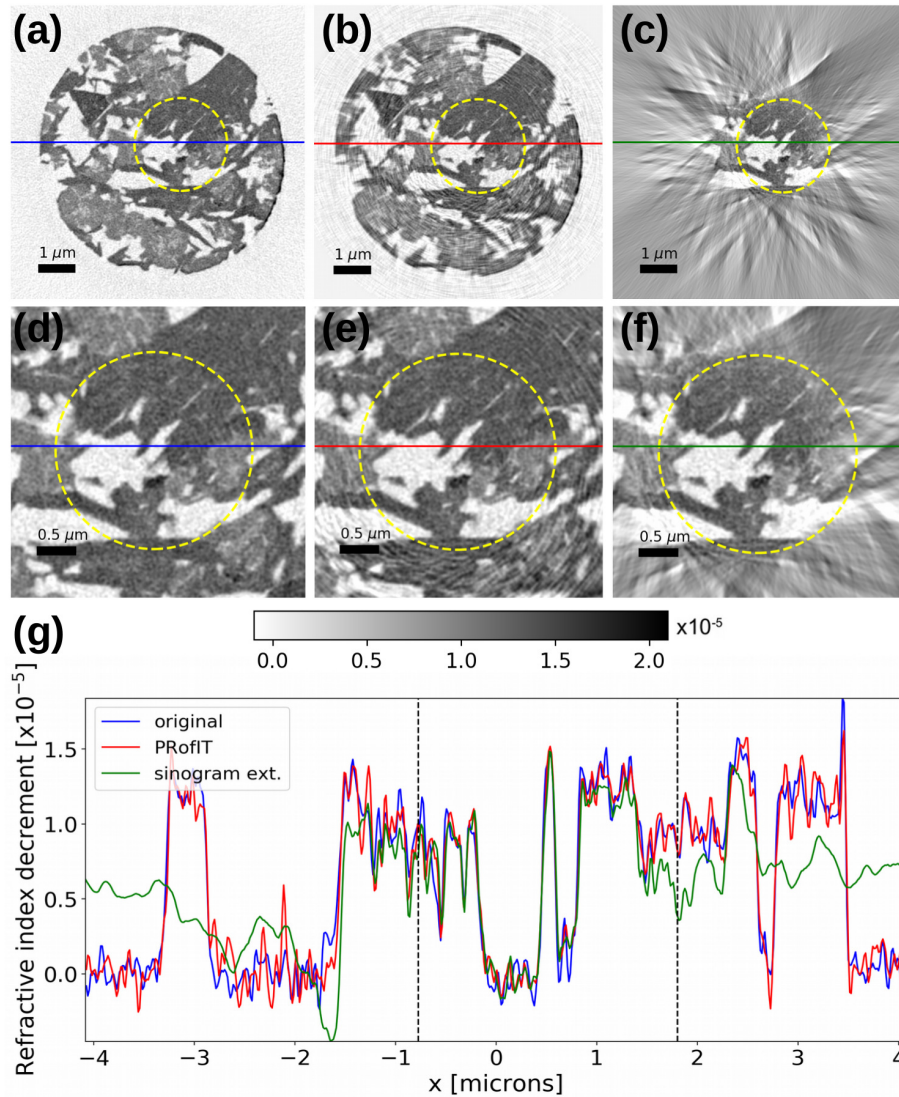


Fig. 6. PProFIT results obtained by truncating the original experimental projections from the 3D volumes of the FCC catalyst sample. (a) Reconstructed slice from non-truncated ptychographic projections. (b) Reconstructed slice from truncated projection using the PProFIT approach with four levels. (c) Reconstructed slice from truncated projections using the sinogram extension approach. An offset of 0.65×10^{-5} was added to the gray level in (c) to compensate for the loss of quantitative contrast of the approach. (d), (e) and (f) show the zoomed-in images of the corresponding ROIs reconstructed in (a), (b) and (c), respectively. The yellow dashed circles represent the region-of-interest. (g) The gray level profiles across the blue, red and green lines in (a), (b), and (c), respectively. The dashed black lines limit the region-of-interest. The colormap of the images is given in units of refractive index decrement δ .

mass density were obtained assuming that the ratio between the atomic mass (A) and the number of electrons, given by the atomic number (Z), in each material can be approximated to 2. Thus, the refractive index decrement can be written as [42]:

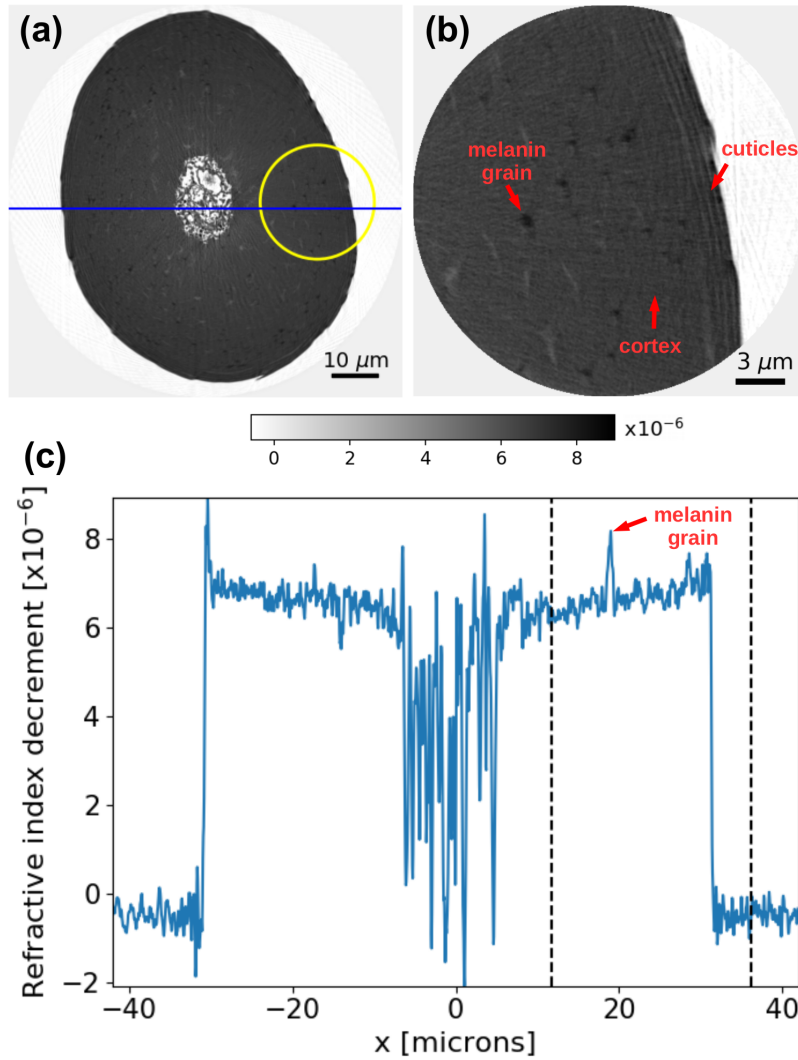


Fig. 7. 3D volume of the hair shaft reconstructed using PProFIT with 2 levels decomposition. (a) Reconstructed slice displaying the entire hair cross section. The gray level is given in units of refractive index decrement δ . The yellow circle highlights the off-centered ROI. (b) Zoom-in of the ROI where the red arrows indicate the cuticles, one melanin grain, and a part of the cortex. (c) Gray level profile across the solid blue line in (a), which crosses a melanin grain as indicated by the red arrow. The dashed lines limit the region-of-interest.

$$\delta \approx 1.35 \times 10^{-6} \rho \lambda^2, \quad (4)$$

where δ is the refractive index decrement, λ is the wavelength in units of Å and ρ is in units of g/cm³. Solving Eq. (4) for ρ , we can obtain the mass density from the gray level values of the reconstructed image. This obviously fails for the hydrogen, leading to a precision of about 10% in the estimates, which we defined as experimental errors of the mass density estimates.

The mass density of the melanin grains is interesting because it is very difficult to obtain in native condition inside the hair cortex. The mass density of the melanin *Sepia Officialis* is 1.7 ± 0.1 g/cm³ [43]. Such a value deviates only about 6% of our estimate. Concerning the hair

cortex, it is well known that it is mostly composed of keratin. The α -keratin has a density of 1.32 g/cm^3 [44], of which our estimation of mass density from the hair cortex deviates by less than 2%.

6. Conclusion

We presented an approach of pseudo region-of-interest tomography that enables the reconstruction of a ROI of a larger sample without the artifacts commonly encountered in local tomography. Because of that, high-resolution images of the ROI can be reconstructed with quantitative capabilities. We do not use only local data, the regions outside the ROI are coarsely sampled in angle using a different scheme of projection acquisition. The results obtained with truncated experimental projections from the catalyst confirmed that PProFIT is a stable approach and preserves the quantitative information of the images. An experimental demonstration was presented, where a ROI of a hair shaft was reconstructed allowing the estimation of the mass density of some hair component, such as the cortex and the pigment melanin with high sensitivity.

We also confirmed that the minimum number of projections must be estimated based on the entire object size and not only on the ROI size, which means that the number of projections M should be $M > (\pi/2) \times (D/\Delta r) + 1$ even for region-of-interest tomography. Based on the analysis of the band region of the Radon transform, we showed this is the required number of projections to avoid aliasing errors that disturb the high frequency information and, consequently, reduce the spatial resolution of the reconstructed tomographic slice.

Compared to the method presented in [11], which combines a low-resolution overview with high-resolution interior projections, PProFIT provides advantages in the postprocessing of projections, namely easier registration and removal of constant and linear phase terms, because the global and interior projections are measured with the same technique and with the same resolution. Another advantage is that PProFIT acquires all the tomographic data in one experiment, whereas the method in [11] requires the combination of the results of two experiments carried out with different techniques, but with similar contrast mechanism. Additionally interpolation artifacts of the low-resolution tomogram are avoided. Finally, unlike the approach of [11], PProFIT provides reconstructions in a direct non-iterative computation, which reduces significantly the computational requirements.

A big advantage of PProFIT is that the region outside the ROI is acquired in the same way as the ROI and with same pixel size. The latter provides a smooth quality transition between the ROI and the external region, which helps with the registration of the projections. Additionally, the level L3 projections, which contain regions of air outside the object, can be used as phase references for absolute phase shifts calibration. This is used to correct for the typical linear phase ramp of the ptychographic projections. This represents an important advantage relative to other approaches like data completion or sinogram extension which are not quantitative without *a priori* knowledge. The PProFIT approach is not a fully local tomography approach because the object density is reconstructed from a combination of truncated and normal projections. However, it can help to reduce the scanning time when only a part of the sample is of interest without the need to scan the full field-of-view covering the entire object for all the tomographic angles.

Appendix A. Estimate of spatial resolution of the reconstructed images in Fig. 6

We estimated the spatial resolution of the reconstructed images in Fig. 6 within the ROI using the Fourier Shell Correlation (FSC) method [45]. Figure 8 displays the resulting curves. The spatial resolution is estimated from the division of the pixel size by the abscissa value of the intersection between the correlation curves with the 1/2 bit threshold curve. Figure 8 displays the resulting FSC curves for the ground truth, PProFIT, and Sinogram extension reconstructions. We notice that there is no substantial change in spatial resolution from one method to another. Since the

intersection was at the abscissa value of ~ 0.365 , we obtained an estimate of spatial resolution of $\sim 39\text{nm}$ for all images.

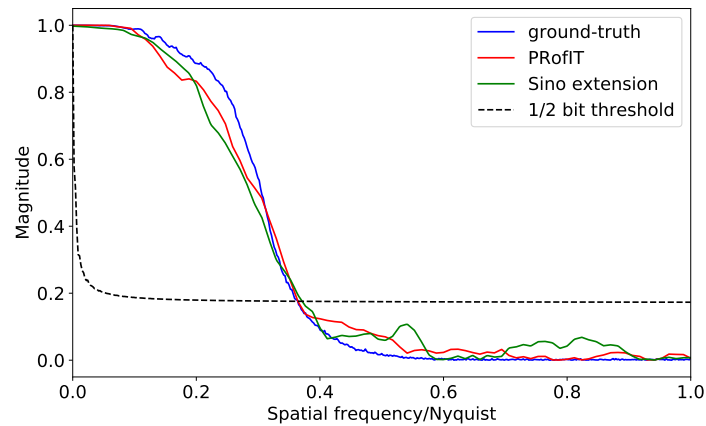


Fig. 8. Fourier Shell correlation curve obtained for the images in Fig. 6 to estimate of spatial resolution of the reconstructions. All curves intersect the threshold curve at about the same value of ~ 0.365 of the axis of abscissae. The pixel size of figures is 14.3 nm .

Funding

Swiss National Science Foundation (SNF) (137772,145056); Competence Centre for Materials Science and Technology (CCMX) of the ETH-Board, Switzerland.

Acknowledgments

We thank X. Donath for technical support at the cSAXS beamline.